Journal of Computational Physics 229 (2010) 2236–2248

Contents lists available at ScienceDirect

Journal of Computational Physics

journal homepage: www.elsevier.com/locate/jcp

An adaptive continuation-multigrid method for the balanced vortex model ☆

Ye Chen, Scott R. Fulton *

Department of Mathematics, Clarkson University, Potsdam, NY 13699-5815, USA

ARTICLE INFO

Article history:
Received 11 August 2009
Received in revised form 17 November 2009
Accepted 21 November 2009
Available online 26 November 2009

Keywords:
Multigrid
Monge-Ampere
Balanced vortex
Continuation

ABSTRACT

Obtaining solutions of the Eliassen balanced vortex model requires solving an invertibility relation, which is a nonlinear elliptic problem of the Monge-Ampere type. Multigrid techniques for this problem are investigated. An adaptive algorithm which combines the full multigrid method with continuation in a parameter related to the strength of the forcing is developed. Numerical results demonstrate the efficiency and robustness of this algorithm.

1. Introduction

The balanced vortex model (BVM) of Eliassen [1] studied in [2–5] describes circularly symmetric atmospheric flows in gradient balance. As such, it is a useful theoretical tool for studying the basic dynamics of hurricanes. It is similar to the semigeostrophic model [6], but more complicated due to the cylindrical coordinate and nonlinear balance condition. When formulated in appropriate coordinates (see Section 2.2) the model reduces to a simple predictive (time-dependent) equation for the potential vorticity, and a diagnostic (time-independent) equation of the Monge-Ampere type, from which the corresponding mass and wind fields may be determined. This latter equation is referred to as the *invertibility relation*; an efficient and robust solution method for this equation is the focus of this paper.

Schubert and Alworth [4] solved the invertibility relation on a single grid using point relaxation; however, the convergence was quite slow and thousands of iterations were required. In contrast, Fulton [7] developed a multigrid solver for the related but simpler semigeostrophic invertibility relation which achieved "typical multigrid efficiency", i.e., solution in the work of 5–7 fine-grid relaxation sweeps. The goal of this paper is to extend this multigrid method to develop an efficient and robust solver for the BVM invertibility relation. The paper is organized as follows. Section 2 reviews the formulation of the model, and relaxation schemes appropriate for this problem are detailed in Section 3. Section 4 describes the test problem, and numerical results are given in Section 5 comparing the single grid and multigrid methods. The problem becomes harder to solve as the strength of the forcing increases; an adaptive algorithm which combines the continuation and full multigrid methods is presented in Section 6 and shown to be efficient and robust. Section 7 summarizes our conclusions.

☆ This work was partially supported by the National Science Foundation under Grant No. ATM-0833057.
* Corresponding author. Tel.: +1 315 268 2379; fax: +1 315 268 2371.
E-mail addresses: chenye@clarkson.edu (Y. Chen), fulton@clarkson.edu (S.R. Fulton).

0021-9991/$ - see front matter © 2009 Elsevier Inc. All rights reserved.
doi:10.1016/j.jcp.2009.11.032

2. Model description

A particularly simple formulation of the BVM was introduced in [4], using potential radius and potential temperature as coordinates. In this section we review this formulation in order to put the invertibility relation (10) into context. We also introduce a new form of the inner boundary condition and give the details of the discretization.

2.1. Balanced vortex model

Consider the motion of a circularly symmetric vortex, expressed in cylindrical coordinates with r as the radial coordinate and horizontal velocity components u and v in the radial and tangential directions, respectively. We assume the horizontal scale is such that the curvature of the Earth can be neglected and the corresponding Coriolis parameter f can be regarded as constant. Rather than using physical height for the vertical coordinate, we use the potential temperature θ, defined as the absolute temperature times the factor $(p_0/p)^\kappa$, where p is the pressure, p_0 is a constant reference pressure, and $\kappa = 2/7$. Since θ is the temperature which a parcel of air would have if it were moved adiabatically to where $p = p_0$, it is conserved in adiabatic flow, and its use as a coordinate simplifies the equations of motion. In this coordinate system the total derivative (following the motion) is $D/Dt = \partial/\partial t + u\partial/\partial r + \dot\theta\partial/\partial\theta$ and $\dot\theta = D\theta/Dt$ is the vertical component of velocity.

The vortex is assumed to be in gradient and hydrostatic balance, i.e., the tangential and vertical components of the momentum equation are given by

$$\left(f + \frac{v}{r}\right)v = \frac{\partial M}{\partial r}, \tag{1}$$

and

$$\frac{\partial M}{\partial \theta} = \Pi. \tag{2}$$

Here $\Pi = c_p(p/p_0)^\kappa$ (with c_p the specific heat at constant pressure), and the gradient of the Montgomery potential $M = \theta\Pi + \phi$ (where ϕ is the geopotential) plays the role of the pressure gradient. The gradient balance (1) eliminates gravity-inertia waves but is more accurate than the geostrophic balance used in the quasigeostrophic and semigeostrophic models [8].

In the absence of radial forcing, absolute angular momentum is conserved and the potential radius R, defined (see [2]) by

$$\frac{1}{2}fR^2 = rv + \frac{1}{2}fr^2, \tag{3}$$

is constant following the motion. More generally, we assume that the radial forcing $\dot R = DR/Dt$ (here identified as "friction") is specified. Similarly, we assume that the vertical velocity $\dot\theta = D\theta/Dt$ (here identified as "heating") is specified. Finally, conservation of mass is expressed in terms of the pseudodensity $\sigma = -\partial p/\partial\theta$ by the continuity equation

$$\frac{D\sigma}{Dt} + \sigma\left(\frac{\partial(ru)}{r\partial r} + \frac{\partial\dot\theta}{\partial\theta}\right) = 0. \tag{4}$$

By differentiating (3) one can derive an equation for the absolute vorticity $\eta = f + v/r + \partial v/\partial r$. Combining this with the continuity equation (4) yields

$$\frac{Dq}{Dt} = \frac{1}{\sigma}\frac{\partial}{r\partial r}(fR\dot R) + q\frac{\partial\dot\theta}{\partial\theta}, \tag{5}$$

where $q = \eta/\sigma$ is the potential vorticity. In principle, if q were predicted using (5), since the mass and wind fields satisfy the balance (1) they could be recovered from q, which combines them. In practice this will not work, since the total derivative involves the radial velocity u, which is unbalanced and not predicted.

2.2. Coordinate transformation

The model is simplified considerably by interchanging the roles of r and R, transforming from (r,θ,t) to (R,Θ,T). Here $\Theta = \theta$ and $T = t$, with the new symbols introduced to distinguish partial derivatives $\partial/\partial\theta$ and $\partial/\partial t$ at fixed r from partial derivatives $\partial/\partial\Theta$ and $\partial/\partial T$ at fixed R. Introducing new dependent variables v^*, M^*, and Γ defined by

$$Rv^* = rv, \qquad M^* = M + \frac{1}{2}v^2, \qquad \Gamma = \frac{d\Pi}{dp} = \frac{\kappa\Pi}{p}, \tag{6}$$

the balance assumptions (1) and (2) transform to

$$\frac{f^2 v^*}{f - 2v^*/R} = \frac{\partial M^*}{\partial R}, \tag{7}$$

and

$$\frac{\partial M^*}{\partial \Theta} = \Pi. \tag{8}$$

The potential vorticity equation (5) transforms to the predictive equation

$$\frac{\partial \sigma^*}{\partial T} + \frac{\partial (R\dot{R}\sigma^*)}{R\partial R} + \frac{\partial (\dot{\theta}\sigma^*)}{\partial \theta} = 0, \tag{9}$$

for the *potential pseudodensity* $\sigma^* = f\sigma/\eta$, which is the (scaled) reciprocal of the potential vorticity. This equation contains advection only by the forcings $\dot{R}$ and $\dot{\theta}$, which are regarded as known; thus, the coordinate transformation has rendered the (unbalanced) radial velocity component u implicit. Consequently, (9) may be solved analytically in many cases (see Section 4).

Since the balanced wind and mass fields are combined in σ^*, by the invertibility principle [9] they can be recovered from σ^*. This requires solving the *invertibility relation* [4]

$$\left[f^2 - R^3 \frac{\partial}{\partial R}\left(R^{-3}\frac{\partial M^*}{\partial R}\right)\right]\frac{\partial^2 M^*}{\partial \Theta^2} + \left(\frac{\partial^2 M^*}{\partial R \partial \Theta}\right)^2 + \Gamma\sigma^*\left(f + \frac{2}{f}\frac{\partial M^*}{R\partial R}\right)^2 = 0, \tag{10}$$

for M^*, where Γ depends on M^* via (6) and (8). The appearance of the R^3 and R^{-3} factors in the radial derivative term is a consequence of the coordinate transformation. Once M^* is obtained from (10)—in which σ^* plays the role of the forcing—the balanced wind and mass fields may be obtained from (7) and (8).

Eq. (10) is a Monge-Ampere equation [10], and is elliptic since $\Gamma > 0$ and $\sigma^* > 0$. It is similar to the semigeostrophic invertibility relation solved in [7], but more complicated due to terms which come from the cylindrical geometry. The goal of this paper is to demonstrate an efficient and robust method for its numerical solution.

It is convenient to express M^* in terms of a deviation from a horizontally uniform basic state. To do so, suppose that the phenomenon being studied is confined in lateral extent so that in the far field (large R), σ^* and η are independent of R. With this assumption it can be shown that $\sigma^* = \sigma$ and $\eta = f$, and that M^* is independent of R. The corresponding solution of (10) and the vertical boundary conditions constitutes a horizontally uniform basic state, the variables of which we denote with overbars. To compute it, we specify $\bar{\sigma}$ as a function of Θ only and obtain the other fields via

$$\frac{d\overline{M}^*}{d\Theta} = \overline{\Pi}, \quad \overline{\Pi} = c_p\left(\frac{\bar{p}}{p_0}\right)^{\kappa}, \quad \overline{\Gamma} = \frac{d\overline{\Pi}}{d\bar{p}}, \quad \bar{\sigma} = -\frac{d\bar{p}}{d\Theta}. \tag{11}$$

Then in terms of the deviation $M' = M^* - \overline{M}^*$, the invertibility relation (10) takes the form

$$\left[f^2 - R^3 \frac{\partial}{\partial R}\left(R^{-3}\frac{\partial M'}{\partial R}\right)\right]\left[\frac{\partial^2 M'}{\partial \Theta^2} - \overline{\Gamma}\sigma_0\right] + \left(\frac{\partial^2 M'}{\partial R \partial \Theta}\right)^2 + \Gamma\sigma^*\left(f + \frac{2}{f}\frac{\partial M'}{R\partial R}\right)^2 = 0. \tag{12}$$

For the results reported here we simply take $\overline{\sigma} = \sigma_0 = (p_B - p_T)/(\Theta_T - \Theta_B)$ in terms of the (constant) values of Θ and p at the domain bottom and top.

2.3. Boundary conditions

We wish to solve (12) on the domain $\Omega = [0, R_B] \times [\Theta_B, \Theta_T]$. At the top boundary $\Theta = \Theta_T$, we suppose the pressure p is the constant value p_T, so from (8) we obtain the condition

$$\frac{\partial M'}{\partial \Theta} = 0 \quad \text{at} \quad \Theta = \Theta_T. \tag{13}$$

At the bottom boundary $\Theta = \Theta_B$, assuming the geopotential vanishes ($\phi = 0$), from the definition of M^* and (8) we obtain

$$\left(f^2 + \frac{2}{R}\frac{\partial M'}{\partial R}\right)\left(\Theta\frac{\partial M'}{\partial \Theta} - M'\right) + \frac{1}{2}\left(\frac{\partial M'}{\partial R}\right)^2 = 0 \quad \text{at} \quad \Theta = \Theta_B. \tag{14}$$

At the outer boundary ($R = R_B$) we assume that $M^* = \overline{M}$, so the outer boundary condition is simply

$$M' = 0 \quad \text{at} \quad R = R_B. \tag{15}$$

At the inner boundary ($R = 0$), Schubert and Alworth [4] used the symmetry condition $\partial M'/\partial R = 0$. Here, we use instead the limiting form of the invertibility relation at $R = 0$. We refer to (12) as the interior invertibility relation (in the interior $0 < R < R_B$). Since $\partial M'/\partial R = 0$ at $R = 0$, we have $\partial^2 M'/\partial R \partial \Theta = 0$ at $R = 0$, and by L'Hôpital's Rule

$$\lim_{R\to 0}\frac{\partial M'}{R\partial R} = \frac{\partial^2 M'}{\partial R^2}, \tag{16}$$

so

$$\lim_{R\to 0}\left[f^2 - R^3\frac{\partial}{\partial R}\left(R^{-3}\frac{\partial M'}{\partial R}\right)\right] = \lim_{R\to 0}\left[f^2 - \frac{\partial^2 M'}{\partial R^2} + \frac{3\partial M'}{R\partial R}\right] = f^2 + 2\frac{\partial^2 M'}{\partial R^2}. \tag{17}$$

Therefore, taking the limit as $R \to 0$ in (12) yields the inner invertibility relation

$$\overline{\Gamma}\sigma_0 - \frac{\partial^2 M'}{\partial \Theta^2} = \Gamma\sigma^*\left(1 + \frac{2}{f^2}\frac{\partial^2 M'}{\partial R^2}\right) \quad \text{at} \quad R = 0. \tag{18}$$

2.4. Discretization

The equations are discretized on a grid defined by $R_i = i\Delta R$ $(i = 0, 1, 2, \ldots, N_R)$ and $\Theta_j = \Theta_B + j\Delta\Theta$ $(j = -1, 0, 1, 2, \ldots, N_\Theta + 1)$, where $\Delta R = R_B/N_R$ and $\Delta\Theta = (\Theta_T - \Theta_B)/N_\Theta$. Ghost points at $j = -1$ and $j = N_\Theta + 1$ are added in the Θ-direction to handle the vertical boundary conditions.

Given the form of the radial derivative term in (12), it is tempting to discretize it in "flux form", evaluating the "flux" $R^{-3}\partial M'/\partial R$ at the midpoints (between grid points). However, it can be shown [11] that the corresponding truncation error is unbounded as $R \to 0$. Consequently, we follow [4] and expand this term as

$$R^3\frac{\partial}{\partial R}\left(R^{-3}\frac{\partial M'}{\partial R}\right) = \frac{\partial^2 M'}{\partial R^2} - \frac{3}{R}\frac{\partial M'}{\partial R}, \tag{19}$$

before discretizing it. The invertibility relation is discretized by using second-order central finite differences. More general finite difference discretizations are considered in [11] (they give slightly smaller truncation error or solution error, but are twice as expensive as the discretization discussed here). Following [4], the discrete version of the invertibility relation becomes

$$\frac{f^2 R_i^2\left(A_{ij}B_{ij} - C_{ij}^2\right)}{\Gamma_{ij}D_{ij}^2\Delta\Theta^2} = \sigma_{ij}^*, \quad i = 1, 2, \ldots, N_R - 1, \quad j = 0, 1, \ldots, N_\Theta, \tag{20}$$

$$\frac{f^2\Delta R^2 B_{ij}}{\Gamma_{ij}\Delta\Theta^2\left(f^2\Delta R^2 + 4M'_{i+1,j} - 4M'_{ij}\right)} = \sigma_{ij}^*, \quad i = 0, \quad j = 0, 1, \ldots, N_\Theta. \tag{21}$$

Here,

$$A_{ij} := 2\left(M'_{ij} - a_{ij}\right), \tag{22}$$

$$a_{ij} := \frac{1}{2}\left[\left(\frac{3\Delta R}{2R_i} + 1\right)M'_{i-1,j} - \left(\frac{3\Delta R}{2R_i} - 1\right)M'_{i+1,j} - f^2\Delta R^2\right], \tag{23}$$

$$B_{ij} := 2\left(M'_{ij} - b_{ij}\right), \tag{24}$$

$$b_{ij} := \frac{1}{2}\left(M'_{ij+1} + M'_{ij-1} - \overline{\Gamma}_j\sigma_0\Delta\Theta^2\right), \tag{25}$$

$$C_{ij} := \frac{1}{4}\left(M'_{i+1,j+1} - M'_{i+1,j-1} - M'_{i-1,j+1} + M'_{i-1,j-1}\right), \tag{26}$$

$$D_{ij} := f^2 R_i\Delta R + M'_{i+1,j} - M'_{i-1,j}. \tag{27}$$

The discrete boundary conditions are

$$M'_{i,N_\Theta+1} = M'_{i,N_\Theta-1}, \quad i = 0, 1, 2, \ldots N_R - 1, \tag{28}$$

$$M'_{i,-1} = \frac{2\Delta\Theta}{\Theta_B}\left[\frac{R_i\left(M'_{i+1,0} - M'_{i-1,0}\right)^2}{8f^2\Delta R^2 R_i + 8\Delta R\left(M'_{i+1,0} - M'_{i-1,0}\right)} - M'_{i,0}\right] + M'_{i,1}, \quad i = 1, 2, 3, \ldots, N_R - 1, \tag{29}$$

$$M'_{0,-1} = M'_{0,1} - \frac{2\Delta\Theta}{\Theta_B}M'_{0,0}, \tag{30}$$

$$M'_{N_R j} = 0, \quad j = -1, 0, 1, 2, \ldots, N_\Theta + 1. \tag{31}$$

To solve this (nonlinear) algebraic system, an iterative method is needed.

3. Relaxation

In this section, three relaxation schemes are presented: point relaxation, R-line relaxation, and Θ-line relaxation. Numerical results are shown in Section 5.

3.1. Point relaxation

Schubert and Alworth [4] solved the discrete invertibility relation (on a single grid) by a point relaxation scheme which can be formulated as follows. Suppose we have an approximation of M', but this approximation does not satisfy (20) at a point (i,j). Keeping the values of M' at the surrounding points unchanged, we update the value of $M'_{i,j}$ so that (20) is satisfied at the point (i,j). Viewed as an equation in the single variable $M'_{i,j}$, the equation (20) is quadratic; since $C_{i,j}$ and $D_{i,j}$ are independent of $M'_{i,j}$, we can write it in the form

$$\left(M'_{i,j} - a_{i,j}\right)\left(M'_{i,j} - b_{i,j}\right) = c_{i,j}, \tag{32}$$

where $c_{i,j} = \left(f^2 R_i^2 C_{i,j}^2 + D_{i,j}^2 \Delta\Theta^2 \Gamma_{i,j}\sigma^*_{i,j}\right)/\left(4f^2 R_i^2\right)$. Note that $c_{i,j} > 0$. Solving (32) yields

$$M'_{i,j} = \frac{1}{2}\left[a_{i,j} + b_{i,j} \pm \sqrt{(a_{i,j} - b_{i,j})^2 + 4c_{i,j}}\right]. \tag{33}$$

To ensure the absolute vorticity is positive, we must have $M'_{i,j} - a > 0$. Choosing the larger root in (33) (+ sign) will guarantee this. Thus, the point relaxation scheme for the interior grid point (i,j) is

$$M'_{i,j} \leftarrow \frac{1}{2}\left[a_{i,j} + b_{i,j} + \sqrt{(a_{i,j} - b_{i,j})^2 + 4c_{i,j}}\right], \tag{34}$$

where $i = 1, 2, 3, \ldots, N_R - 1$ and $j = 0, 1, 2, \ldots, N_\Theta$. Similarly, on the inner boundary, solving the discrete equation (21) for $M'_{i,j}$ yields

$$M'_{i,j} \leftarrow M'_{i+1,j} + \frac{1}{4}f^2\Delta R^2 - \frac{f^2\Delta R^2 B_{i,j}}{4\Gamma_{i,j}\sigma^*_{i,j}}, \tag{35}$$

where $i = 0$ and $j = 0, 1, 2, \ldots, N_\Theta$.

A relaxation sweep consists of updating $M'_{i,j}$ by (34) and (35) at interior points in lexicographic order and the inner boundary points, respectively. After updating all interior points and inner boundary points, the ghost points are updated using (28)–(30). When used as a solution method on a single grid [4], this point relaxation works but the convergence is exceedingly slow.

When used as a smoother in a multigrid method, this point relaxation also performs poorly, since the problem is highly anisotropic. To see this, the invertibility relation (12) linearized about the basic state given by (11) takes the form

$$-\overline{\Gamma}\sigma_0\left(\frac{\partial^2 M'}{\partial R^2} + \frac{\partial M'}{R\partial R}\right) - f^2\frac{\partial^2 M'}{\partial\Theta^2} = f^2\overline{\Gamma}(\sigma^* - \sigma_0). \tag{36}$$

Considering only the principal (second-order) terms, this problem would appear nearly isotropic on a grid with mesh spacing $(\Delta R, \Delta\Theta)$ if the ratio $\lambda = (\overline{\Gamma}\sigma_0/\Delta R^2)/(f^2/\Delta\Theta^2)$ is approximately 1. However, using values from [4] gives $\lambda \gg 1$ as shown in Fig. 1, so the coupling is much stronger in the R-direction than in the Θ-direction. Since λ varies strongly with Θ, changing the mesh spacing ΔR or $\Delta\Theta$ to make $\lambda \approx 1$ is not possible. Consequently, point relaxation will not work well, a conclusion confirmed by numerical results (see Section 5). The solution here is to use line relaxation.

3.2. R-line relaxation

Since the equation has strong coupling in the R-direction, R-line relaxation should be used. To formulate this scheme, we fix a horizontal R-line indexed by j with $0 \leqslant j \leqslant N_\Theta$. The values $\mathbf{H}_j := \left[M'_{0,j}, M'_{1,j}, \ldots, M'_{N_R j}\right]^T$ are regarded as unknowns, and the values at adjacent R-lines $(j \pm 1)$ are treated as known. From (21), (20) and (31), the equations to be solved for $\mathbf{H}_j$ are

$$F_{0,j}(\mathbf{H}_j) := f^2\Delta R^2 B_{0,j} - \Gamma_{0,j}\sigma^*_{0,j}\Delta\Theta^2\left[f^2\Delta R^2 + 4M'_{1,j} - 4M'_{0,j}\right] = 0, \tag{37}$$

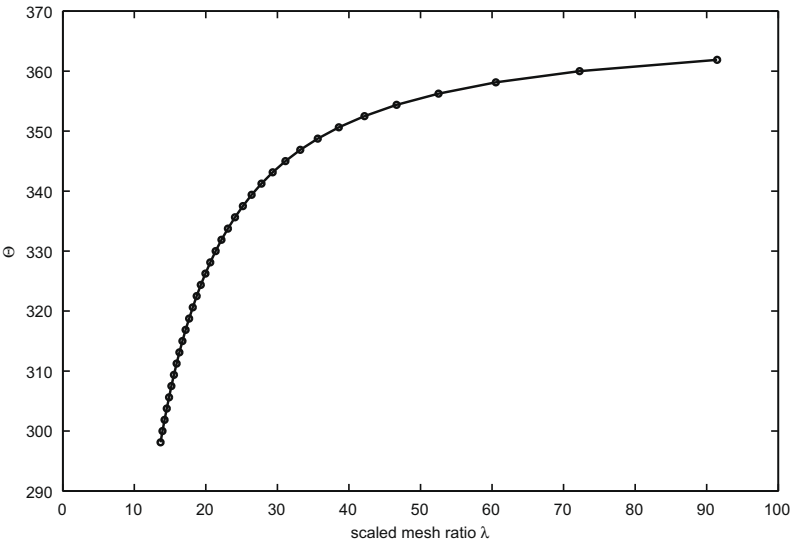

Fig. 1. Anisotropy of the linearized invertibility relation.

$$F_{ij}(\mathbf{H}_j) := f^2 R_i^2 \left(A_{ij}B_{ij} - C_{ij}^2\right) - \Gamma_{ij}\sigma_{ij}^* \Delta\Theta^2 D_{ij}^2 = 0, \quad i = 1, 2, \ldots, N_R - 1, \tag{38}$$

$$F_{N_R j}(\mathbf{H}_j) := M'_{N_R j} = 0. \tag{39}$$

We write the nonlinear system (37)–(39) in vector form as $\mathbf{F}_j(\mathbf{H}_j) = \mathbf{0}$ and solve it (approximately) by one iteration of Newton's method. Additional iterations and modified Newton's methods are not needed, since the role of relaxation here is not to solve the problem but only to smooth the error [12, sec. 5.4]. Computing the Newton iteration is simple because the Jacobian matrix of the vector function $\mathbf{F}_j$ is tridiagonal and diagonally dominant. After doing relaxation on each R-line ($j = 0, 1, 2, \ldots, N_\Theta$), the top and bottom boundary conditions (28)–(30) are applied to set the vertical ghost point values.

3.3. Θ-line relaxation

When the strong coupling only occurs in the R-direction, R-line relaxation will work fine. However, in (12), the coefficients are not constant but varying, and it is possible that strong coupling of unknowns may appear in both the R-direction and the Θ-direction when the nonlinear terms dominate. In this case, Θ-line relaxation is required. Compared to R-line relaxation, Θ-line relaxation is more complicated since the operators are different on the inner boundary and in the interior.

For a given vertical Θ-line indexed by i with $0 \leqslant i < N_R$, the values $\mathbf{V}_i := \left[M'_{i,-1}, M'_{i,0}, \ldots, M'_{i,N_\Theta+1}\right]^T$ $(i = 0, 1, 2, \ldots, N_R - 1)$ are viewed as unknowns, and the values at adjacent Θ-lines $(i \pm 1)$ are regarded as known. From (30), (21) and (28), the equations to be solved for $\mathbf{V}_0$ (the inner boundary, $i = 0$) are

$$G_{0,-1}(\mathbf{V}_0) = \Theta_B M'_{0,1} - \Theta_B M'_{0,-1} - 2\Delta\Theta M'_{0,0} = 0, \tag{40}$$

$$G_{0j}(\mathbf{V}_0) = f^2 \Delta R^2 B_{0j} - \Gamma_{0j}\sigma_{0j}^* \Delta\Theta^2 \left[f^2\Delta R^2 + 4M'_{1j} - 4M'_{0j}\right] = 0, \quad j = 0, 1, \ldots, N_\Theta, \tag{41}$$

$$G_{0,N_\Theta+1}(\mathbf{V}_0) = M'_{0,N_\Theta+1} - M'_{0,N_\Theta-1} = 0. \tag{42}$$

For the interior ($i = 1, 2, 3, \ldots, N_R - 1$), from (29), (20) and (28), the equations to be solved for $\mathbf{V}_i$ are

$$G_{i,-1}(\mathbf{V}_i) = \left[4R_i\Delta R^2 f^2 + 4\Delta R\left(M'_{i+1,0} - M'_{i-1,0}\right)\right]\left[\Theta_B\left(M'_{i,1} - M'_{i,-1}\right) - 2\Delta\Theta M'_{i,0}\right] + R_i\Delta\Theta\left(M'_{i+1,0} - M'_{i-1,0}\right)^2 = 0, \tag{43}$$

$$G_{ij}(\mathbf{V}_i) = f^2 R_i^2 \left(A_{ij}B_{ij} - C_{ij}^2\right) - \Gamma_{ij}\sigma_{ij}^* \Delta\Theta^2 D_{ij}^2 = 0, \quad j = 0, 1, \ldots, N_\Theta, \tag{44}$$

$$G_{i,N_\Theta+1}(\mathbf{V}_i) = M'_{i,N_\Theta+1} - M'_{i,N_\Theta-1} = 0. \tag{45}$$

As before, the nonlinear system $\mathbf{G}_i(\mathbf{V}_i) = \mathbf{0}$ is solved approximately by one Newton iteration; the Jacobian matrices are again tridiagonal and diagonally dominant (once the ghost-point values are eliminated using the boundary conditions). For our

problem, Θ-line relaxation will be used only in combination with R-line relaxation, with one *alternating line relaxation* sweep consisting of one R-line sweep followed by one Θ-line sweep.[1]

4. Test problem

Following Schubert and Alworth [4] we can solve the predictive equation (9) analytically by the method of characteristics as follows. Suppose the flow is frictionless ($\dot{R} = 0$) and the heating is given by

$$\dot{\theta} = Q(R)F(z), \tag{46}$$

where $z(\Theta) = \pi(\Theta - \Theta_B)/(\Theta_T - \Theta_B)$ with $Q(R)$ and $F(z)$ to be specified later. Then (9) becomes

$$\frac{\partial}{\partial \tau}(\dot{\theta}\sigma^*) + F(z)\frac{\partial}{\partial z}(\dot{\theta}\sigma^*) = 0, \tag{47}$$

where $\tau(R,T) = \pi Q(R)T/(\Theta_T - \Theta_B)$. Thus, $\dot{\theta}\sigma^*$ is constant along characteristic curves defined by

$$\frac{dz}{F(z)} = d\tau. \tag{48}$$

Therefore, the characteristic through (z,τ) and $(z_0,0)$ satisfies

$$\dot{\theta}(z,\tau)\sigma^*(z,\tau) = \dot{\theta}(z_0,0)\sigma^*(z_0,0) = \sigma_0\dot{\theta}(z_0,0), \tag{49}$$

where in the last step we have assumed that the flow is motionless at $T = 0$ so $\sigma^* = \sigma_0$ at $\tau = 0$. Therefore, the forcing takes the form

$$\sigma^*(z,\tau) = \sigma_0\frac{F(z_0)}{F(z)}. \tag{50}$$

For the vertical profile $F(z) = \sin(z)$ used by Schubert and Alworth [4] (we will consider other profiles in Section 6), by integration of (48) the solution is

$$z_0(z,\tau) = 2\arctan[e^{-\tau}\tan(z/2)]. \tag{51}$$

The resulting forcing of the invertibility relation is therefore

$$\sigma^*(z,\tau) = \sigma_0\begin{cases} e^{-\tau} & z = 0, \\ (\sin z)^{-1}\sin[2\arctan(e^{-\tau}\tan(z/2))] & 0 < z < \pi, \\ e^{\tau} & z = \pi. \end{cases} \tag{52}$$

For the results reported here we use the values $\Theta_B = 300$ K, $\Theta_T = 360$ K, $p_0 = p_B = 1000$ mb, $p_T = 100$ mb, and $f = 10^{-4}$ s^{-1}. The radial profile of heating is given by $Q(R) = Q_0 e^{-(R/R_0)^2}$ with $R_0 = 250$ km and $Q_0 = 30$ K/day. Unless otherwise specified, each iterative method is halted when the current residual norm is less than 10^{-6} times the initial residual norm.

5. Continuation-multigrid methods

The forcing specified above depends on the time T; when T is large, the forcing is stronger so the invertibility relation is more nonlinear and harder to solve. Consequently, we solve the problem from time $T = 0$ to $T = 96$ h based on a continuation method as follows. The time is divided into a time series $T_i = i\Delta T, i = 0, 1, 2\ldots$, with $\Delta T = 2$ h. The solution at time T_i is used as the initial solution at time T_{i+1}. At each time step, the problem is solved by a multigrid method or on a single grid. First, we reproduced the results in [4] by point relaxation on a single grid with grid size 48×32. After several thousand iterations (at each T_i), it took 233735 seconds[2] to obtain the solution at $T = 96$ h. The solutions obtained for M^* and its derivatives match those in [4] (e.g., see Fig. 7 below). Multigrid methods [13,14] can give much faster convergence with a rate independent of the mesh size. Using multigrid V-cycles to solve at each time T_i in the continuation method gives the *Continuation-Multigrid* (C-MGV) algorithm described below.

The coarse grids are set up by doubling mesh size in both directions; in our tests the coarsest grid is $(N_R, N_\Theta) = (3,2)$. The full approximation scheme (FAS) is used (since the problem is nonlinear) and V(2,1) cycles are used. The fine-to-coarse grid transfers (restriction) are injection for the solution and full weighting for the residual, and the coarse-to-fine transfer (prolongation) is bilinear interpolation for the correction (and bicubic interpolation for the FMG solution transfer in the next section).

[1] We also investigated semi-coarsening, i.e., R-line relaxation with coarsening in Θ only; however, computational results (not shown) indicate this is much less effective for this problem.

[2] The solution times in this paper are reported for the algorithms coded in Matlab on an IBM ThinkPad T60 with Intel Core(TM) 2 Processor T7400.

Point relaxation is much faster with multigrid than on a single grid, taking only 7796 seconds to get the solution. However, this result is far from optimal. We can measure the performance of the multigrid method by the average numerical convergence factor per sweep $\mu_N := (\|r_m\|/\|r_0\|)^{1/[m(\nu_1+\nu_2)]}$, where $\|\cdot\|$ is the discrete L_2 norm, r_0 is the residual before any V-cycles (the initial guess is zero at the beginning or a previous approximate solution obtained in the method) and r_m is the residual after m multigrid V(ν_1, ν_2) cycles. The number m of V-cycles depends on the stopping criterion (see Section 6); typically, 3–6 cycles were needed. The convergence factors are close to 1 (see Fig. 2), and deteriorate as time (forcing strength) increases.

As indicated in Section 3.1, this poor performance is due to the fact that the problem is highly anisotropic. This conclusion is confirmed by the slight improvement obtained when the mesh aspect ratio is changed (see Fig. 2). Since the strong coupling lies in the R-direction, R-line relaxation is appropriate; this reduces the solution time to only 49 seconds. This is 4770 times faster than point relaxation on a single grid, and 159 times faster than point relaxation with multigrid methods.

Although R-line relaxation is effective for small T, when T is large ($T > 82$ h), the convergence factor deteriorates, as shown in Fig. 3. The BVM invertibility relation has variable coefficients which depend on the solution, so one possible cause of the poor convergence in R-line relaxation is that with strong forcing the strong coupling may occur in both the R-direction and the Θ-direction. In this case, alternating line relaxation may help. From Fig. 3, we can see that better convergence factors are obtained when using the alternating line relaxation, especially at large time. At time $T = 96$ h, the convergence factor is

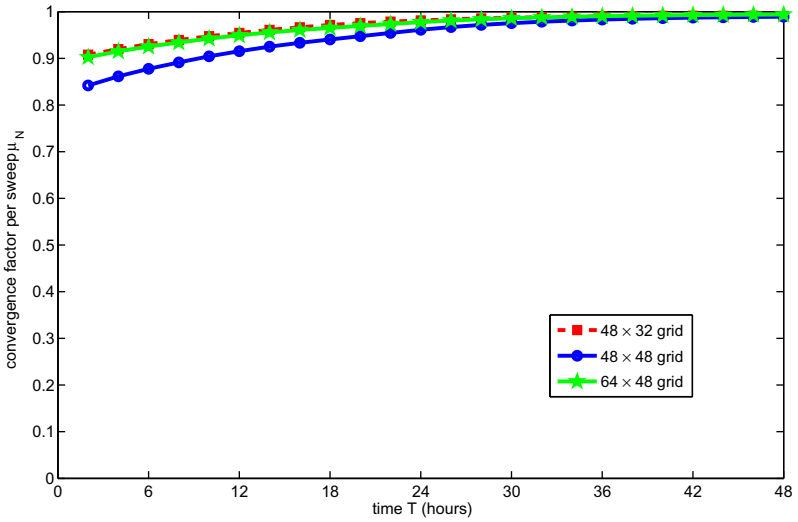

Fig. 2. Numerical convergence factor per sweep for point relaxation.

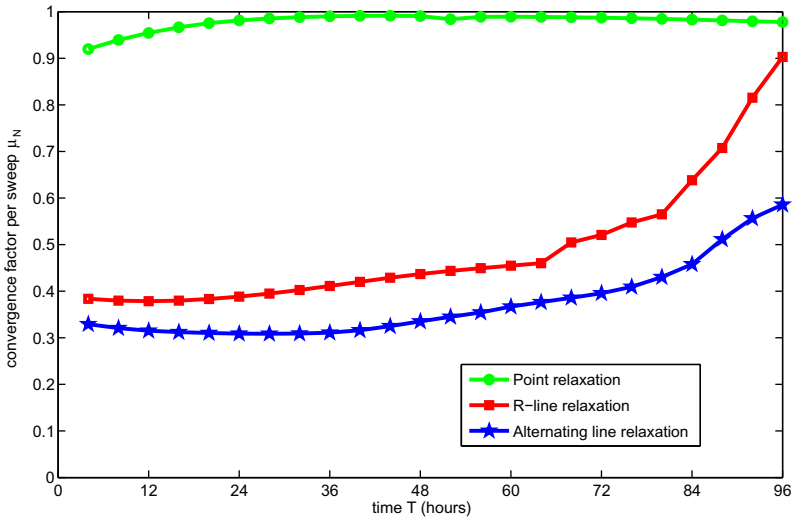

Fig. 3. Numerical convergence factors for line relaxation schemes.

Table 1
Time (in seconds) to solve the invertibility relation to $T = 96$ h using the C-MGV algorithm.

Grid size	R-line	Alternating line
48×32	49	32
96×64	68	51
192×128	302	241
384×256	1517	1193
768×512	6268	5406

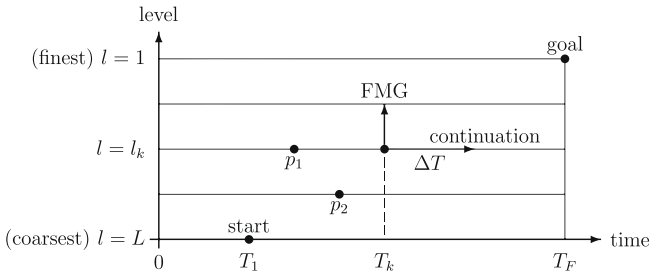

Fig. 4. Basic choices in the C-FMG algorithm at level l_k and time T_k.

0.91 using R-line relaxation only, while alternating line relaxation gives the convergence factor 0.58. Although alternating line relaxation takes twice as much work per sweep as R-line relaxation, the improvement in convergence more than makes up for this, as shown in Table 1.
So, from now on we consider the alternating line relaxation only.

6. Adaptive continuation-FMG methods

In the C-MGV algorithm described above, the final solution at one time T_i is used as the initial approximation for multigrid cycling at the next time T_{i+1}. In contrast, the full multigrid (FMG) method obtains the initial approximation from a coarser grid. For this problem, the FMG method works for small time (e.g., $T \leqslant 46$ h on a 48×32 grid). However, for large time, the FMG method fails, since the forcing is too strong. In this section we combine the FMG method with continuation, a combination we call the C-FMG algorithm. The algorithm proceeds as follows.

Suppose the BVM invertibility relation is to be solved on an $N_R \times N_\Theta$ grid (level $l = 1$) at time $T = T_F$ as shown in Fig. 4. The algorithm is initialized with a solution on the coarsest grid ($l = L$) at some time T_1 (determined by starting with $T = T_F$ and dividing T by two repeatedly until the problem can be solved). From this point, the algorithm steps through times T and levels l toward the goal $T = T_F, l = 1$. The solutions so obtained are indexed by $k = 1, 2, \ldots$, storing the level l_k, time T_k, and corresponding solution (in case the algorithm needs to "back up"). The basic idea is to work on as coarse a grid as possible (l large) for as long as possible (T large), using continuation to move forward in time T, and only using FMG (to the next finer grid) when continuation fails or the final time T_F is reached.[3]

The full details of the algorithm are given in Fig. 5, where the numbered locations reference the discussion below. To illustrate how the algorithm works, suppose that the problem has been solved (by multigrid V-cycles) on level l_k at time T_k (marked ① in Fig. 5). Then as shown in Fig. 4 the approach is as follows:

- Try continuation (marked ②) to the final time T_F, using the solution from the previous time as the initial approximation (make ΔT smaller if needed, marked ③).
- If continuation fails or $T = T_F$, try FMG, i.e., move to the next finer grid using bicubic interpolation (marked ④).
- If FMG fails, back up to a previous solution, on the same level if possible (point p_1) or a coarser level if necessary (point p_2) and try FMG from there (marked ⑤).

In this algorithm, "T small" means $T < 0.1$ h, and "ΔT small" means $\Delta T < 0.01$ h. In each case the multigrid cycling starts with an initial approximation from the previous solution, either at a previous time (continuation) or coarser level (FMG). Alternatively, one could solve for the change from the previous solution and/or use an F-cycle [15].

To determine whether the problem is solved on a given grid, two convergence criteria are considered. One is that multigrid cycling is halted when the residual norm is less than 10^{-6} times the initial residual norm on that grid; we refer to this

[3] If the solution is desired on the finest level at more than one time, this combination of continuation and FMG can be extended accordingly.

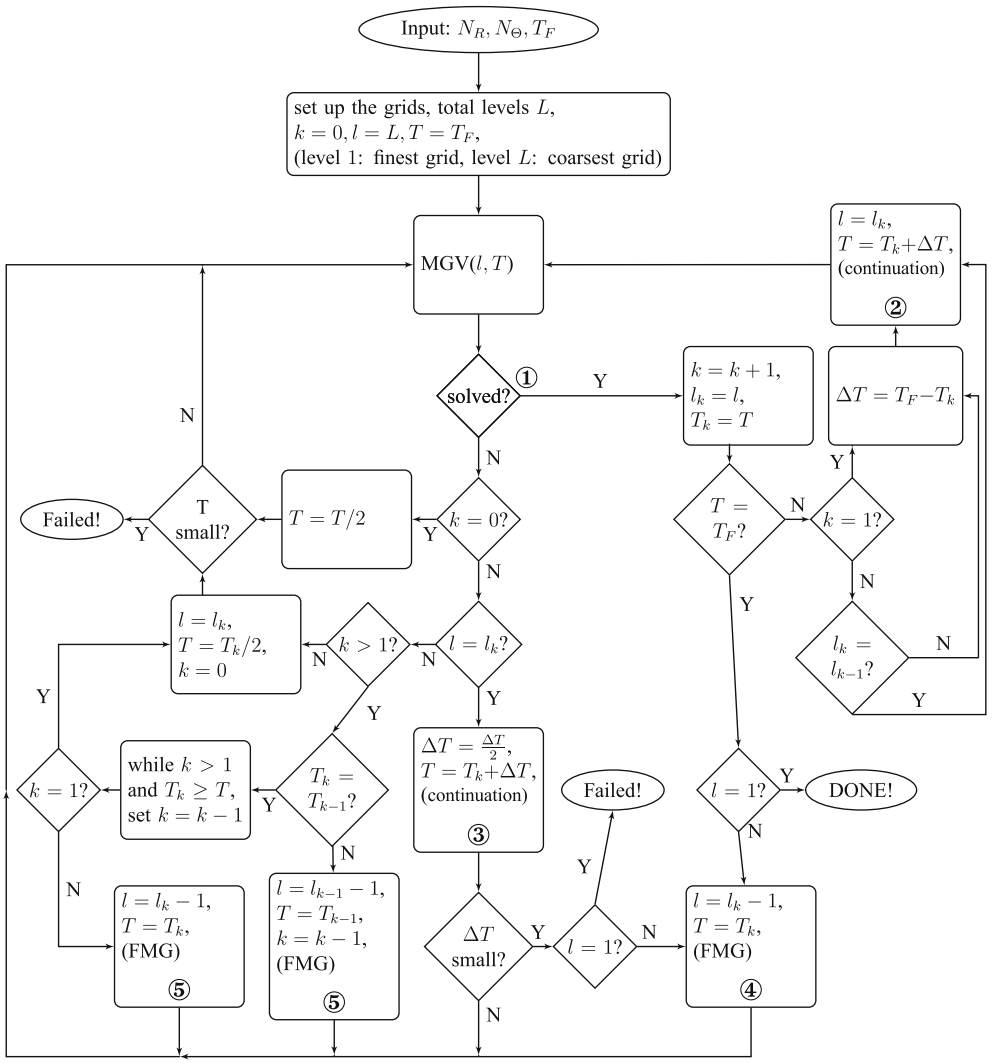

Fig. 5. The C-FMG algorithm.

as the *adaptive C-FMG* algorithm (AC-FMG). The other uses the same criterion on the coarsest grid, but on finer grids the problem is considered solved when the residual norm is less than half of the estimated truncation error norm. For this problem that estimate on grid level l is

$$\tau^l \approx \frac{1}{3}\left(\hat{f}^{l+1} - \widehat{I}_l^{l+1} f^l\right),$$

where f^l is the fine-grid forcing, $\hat{f}^{l+1}$ is the FAS right-hand side on the next coarser grid (level $l+1$), and $\widehat{I}_l^{l+1}$ denotes transfer from fine to coarse *by injection*; for details, see [16]. With this stopping criterion, the method is referred to as the *fully adaptive C-FMG* algorithm (FAC-FMG). In either case, if the convergence criterion is not satisfied in 15 V-cycles (typically 3–6 are

Table 2
Time (in seconds) to solve the invertibility relation to $T = 96$ h using three different algorithms.

Grid size	C-MGV	AC-FMG	FAC-FMG
48×32	32	6	4
96×64	51	10	6
192×128	241	20	9
384×256	1193	62	20
768×512	5406	221	61
1536×1024	Failed	775	229

enough), or the residual norm on the grid increases by a factor of 10^3, the solution at that time and level is deemed to have failed, and the algorithm tries another time or level as described above.

The numerical results of the C-FMG algorithms are listed in Table 2. They work on very high resolution, while the C-MGV may fail. The AC-FMG works 5 times faster than the C-MGV (the same stopping criterion used) on a low resolution grid; when the resolution is high, the AC-FMG works 12-24 times faster than the C-MGV. The FAC-FMG is even faster, showing that the convergence tolerance (10^{-6}) used in the other two algorithms is smaller than needed. So, from now on we will focus on the FAC-FMG.

One important feature of the FAC-FMG is that the method (continuation or FMG) and time are chosen automatically by the algorithm itself, which should make it more robust. To test the robustness, we solved the invertibility relation for different forcings. All the experiments done so far were based on the heating profile $F(z) = \sin(z)$ used by Schubert and Alworth [4]. Since $F'(z) \neq 0$ near the top of the domain ($z = \pi$), this heating generates an intense upper-level anticyclone (e.g., Fig. 7, top right panel). Since this is physically unrealistically [17], we now consider the profile $F(z) = az(z - b\pi)^2$, where a and b are constants. With $b \approx 1$ this profile satisfies $F'(z) \approx 0$ near the top ($z = \pi$), as shown in Fig. 6 for the choices of a and b given in Table 3. The resulting solution is more realistic (see Fig. 7, bottom right panel).

To derive the corresponding forcing σ^*, we can integrate (48) to show that the characteristic through (z, τ) and $(z_0, 0)$ satisfies

$$z_0(z,\tau) = \begin{cases} 0 & z = 0, \\ b\pi w/(1+w) & 0 < z < \pi, \\ \pi & z = \pi, \end{cases} \tag{53}$$

where $w = w(z, \tau)$ is the inverse of

$$z(w) = \frac{w}{b\pi - w} \exp\left(\frac{w}{b\pi - w} - ab^2\pi^2\tau\right), \tag{54}$$

which can be computed using the Lambert W-function [18,19]. The corresponding forcing σ^* is then given by (50).

Fig. 7 shows the normalized forcing σ^*/σ_0 and corresponding tangential wind v, computed from the solution M^* of the invertibility relation via (6), (7) and (3) for profiles A and D of Fig. 6. Profile D is more realistic in that the upper-level anticyclone is weaker and does not extend to the top boundary. However, this case is also considerably harder to compute, since $\sigma^*/\sigma_0 \ll 1$ near the corner $(R, \Theta) = (0, \Theta_B)$, making the invertibility relation nearly non-elliptic there. This is reflected in the time required to compute the solution as shown in Table 3. When the resolution is low, the C-MGV algorithm can also solve the problem—provided that the time step is small enough. But the appropriate time step is unknown unless many times are tried. After many experiments, the time step needed is 2 h for profiles A and B, 1 h for profile C, and 0.02 h for profile D.

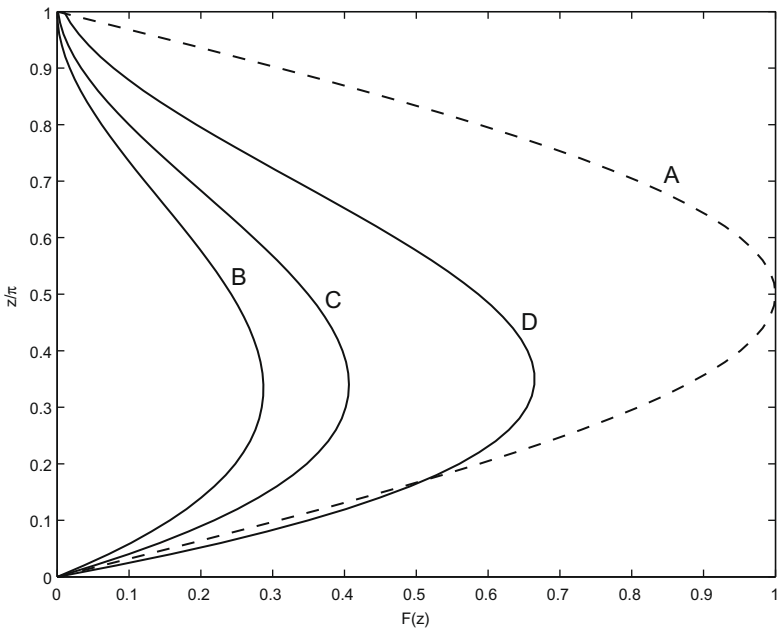

Fig. 6. Vertical profiles of heating as given in Table 3.

Table 3
Time (in seconds) to solve the invertibility relation to $T = 96$ h for different heating profiles.

	48×32 grid		192×128 grid	
Heating profile $F(z)$	C-MGV	FAC-FMG	C-MGV	FAC-FMG
A: $\sin(z)$	32	4	241	9
B: $z(z-\pi)^2/16$	28	1	329	4
C: $z(z-1.02\pi)^2/12$	31	2	377	5
D: $z(z-1.05\pi)^2/8$	2386	14	30,764	283

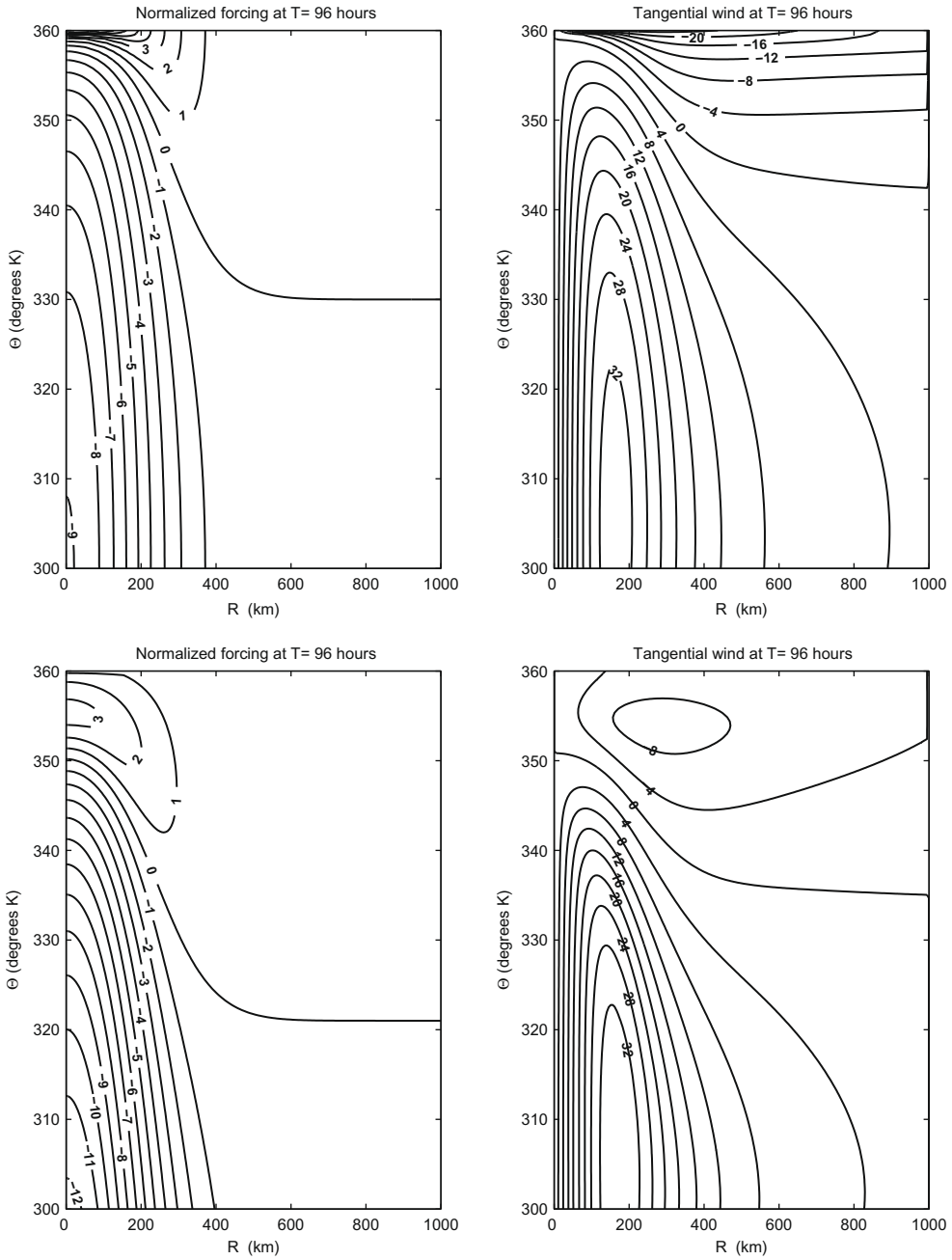

Fig. 7. Results for heating profiles A (top two panels) and D (bottom two panels). The left panels show the normalized forcing σ^*/σ_0 with contours labeled by $\log_2(\sigma^*/\sigma_0)$. The right panels show the tangential wind v in m/s.

7. Summary and conclusions

Efficient and robust multigrid methods have been developed for the invertibility relation of the BVM. Since the problem is highly anisotropic, and the strong coupling occurs in both directions, the numerical results show that the alternating line relaxation is a good smoother for this problem. A continuation-multigrid algorithm (C-MGV) which combines continuation in time (strength of forcing) and multigrid V-cycles works well, solving the problem several orders of magnitude faster than single-grid relaxation.

For small time (weak forcing), the problem can be solved by the full multigrid (FMG) method directly, but for large time (strong forcing), the FMG method will fail. However, combining continuation and FMG yields an algorithm which is efficient and robust. The fully adaptive version (the FAC-FMG algorithm) described here chooses the method (continuation or FMG) and size of continuation step automatically, and determines the convergence tolerance based on the truncation error as estimated during multigrid processing. Numerical results show this algorithm is quite fast and works for different cases of forcing, including some for which the problem is nearly non-elliptic. This method should extend to other balanced models with invertibility relations of the Monge-Ampere type.

Acknowledgment

The authors thank Wayne Schubert, Peter Turner, Kathleen Fowler, Joseph Skufca, and Brian Helenbrook for helpful discussions.

References

[1] A. Eliassen, Slow thermally or frictionally controlled meridional circulation in a circular vortex, Astrophys. Norv. 5 (1952) 19–60.
[2] W.H. Schubert, J.J. Hack, Transformed Eliassen balanced vortex model, J. Atmos. Sci. 40 (1983) 1571–1583.
[3] J.J. Hack, W.H. Schubert, Nonlinear response of atmospheric vortices to heating by organized cumulus convection, J. Atmos. Sci. 43 (1986) 1559–1573.
[4] W.H. Schubert, B.T. Alworth, Evolution of potential vorticity in tropical cyclones, Q.J. Roy. Meteorol. Soc. 113 (1987) 147–162.
[5] W.H. Schubert, S.R. Fulton, R.A. Hertenstein, Balanced atmospheric response to squall lines, J. Atmos. Sci. 46 (1989) 2478–2483.
[6] B.J. Hoskins, The geostrophic momentum approximation and the semi-geostrophic equations, J. Atmos. Sci. 32 (1975) 233–242.
[7] S.R. Fulton, Multigrid solution of the semigeostrophic invertibility relation, Mon. Wea. Rev. 117 (1989) 2059–2066.
[8] J.C. McWilliams, P.R. Gent, Intermediate models of planetary circulations in the atmosphere and ocean, J. Atmos. Sci. 37 (1980) 1657–1678.
[9] B.J. Hoskins, M.E. McIntyre, A.W. Robertson, On the use and significance of isentropic potential vorticity maps, Q.J. Roy. Meteorol. Soc. 111 (1985) 877–946.
[10] R. Courant, D. Hilbert, Methods of Mathematical Physics, vol. II, Wiley-Interscience, New York, 1962.
[11] Y. Chen, Efficient and robust solvers for Monge-Ampere equations, Ph.D. Thesis, Clarkson University, Potsdam, New York, 2009.
[12] K. Stüben, U. Trottenberg, Multigrid methods: Fundamental algorithms, model problem analysis and applications, in: W. Hackbusch, U. Trottenberg (Eds.), Multigrid methods, Lecture Notes in Mathematics, vol. 960, Springer-Verlag, 1982, pp. 1–176.
[13] A. Brandt, Multi-level adaptive solutions to boundary-value problems, Math. Comput. 31 (1977) 333–390.
[14] U. Trottenberg, C. Oosterlee, A. Schüller, Multigrid, Academic Press, San Diego, 2001.
[15] I. Yavneh, J.C. McWilliams, Robust multigrid solution of the shallow-water balance equations, J. Comput. Phys. 119 (1995) 1–15.
[16] S.R. Fulton, On the accuracy of multigrid truncation error estimates, Elec. Trans. Numer. Anal. 15 (2003) 29–37.
[17] W.M. Frank, Large-scale characteristics of tropical cyclones, Mon. Wea. Rev. 110 (1982) 572–586.
[18] D.A. Barry, J.Y. Parlange, L. Li, Analytical approximations for real values of the Lambert W-function, Math. Comput. Simul. 53 (2000) 95–103.
[19] F. Chapeau-Blondeau, A. Monir, Numerical evaluation of the Lambert W-function and application to generation of generalized Gaussian noise with exponent 1/2, IEEE Trans. Signal Process. 50 (2002) 2160–2165.